

Clark University

Clark Digital Commons

---

Biology

Faculty Works by Department and/or School

---

1-1-2023

## Comparative Genomic Analysis of 31 Phytophthora Genomes Reveals Genome Plasticity and Horizontal Gene Transfer

Brent A. Kronmiller  
*Oregon State University*

Nicolas Feau  
*University of British Columbia*

Danyu Shen  
*Nanjing Agricultural University*

Javier F. Tabima  
*Clark University, jtabima@clarku.edu*

Shahin S. Ali  
*USDA, Agricultural Research Service*

See next page for additional authors [https://commons.clarku.edu/faculty\\_biology](https://commons.clarku.edu/faculty_biology)



Part of the [Geography Commons](#)

---

### Repository Citation

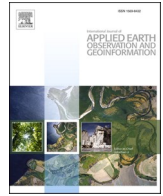
Kronmiller, Brent A.; Feau, Nicolas; Shen, Danyu; Tabima, Javier F.; Ali, Shahin S.; Armitage, Andrew D.; Arredondo, Felipe; Bailey, Bryan A.; Bollmann, Stephanie R.; Dale, Angela; Harrison, Richard J.; Hrywkiw, Kelly; Kasuga, Takao; McDougal, Rebecca; Nellist, Charlotte F.; Panda, Preeti; Tripathy, Sucheta; Williams, Nari M.; Ye, Wenwu; Wang, Yuanchao; Hamelin, Richard C.; and Grünwald, Niklaus, "Comparative Genomic Analysis of 31 Phytophthora Genomes Reveals Genome Plasticity and Horizontal Gene Transfer" (2023). *Biology*. 1.  
[https://commons.clarku.edu/faculty\\_biology/1](https://commons.clarku.edu/faculty_biology/1)

This Article is brought to you for free and open access by the Faculty Works by Department and/or School at Clark Digital Commons. It has been accepted for inclusion in Biology by an authorized administrator of Clark Digital Commons. For more information, please contact [larobinson@clarku.edu](mailto:larobinson@clarku.edu), [cstebbins@clarku.edu](mailto:cstebbins@clarku.edu).

---

## Authors

Brent A. Kronmiller, Nicolas Feau, Danyu Shen, Javier F. Tabima, Shahin S. Ali, Andrew D. Armitage, Felipe Arredondo, Bryan A. Bailey, Stephanie R. Bollmann, Angela Dale, Richard J. Harrison, Kelly Hrywkiw, Takao Kasuga, Rebecca McDougal, Charlotte F. Nellist, Preeti Panda, Sucheta Tripathy, Nari M. Williams, Wenwu Ye, Yuanchao Wang, Richard C. Hamelin, and Niklaus Grünwald



# A super-ensemble approach to map land cover types with high resolution over data-sparse African savanna landscapes

Lei Song<sup>a,\*</sup>, Anna Bond Estes<sup>b,c</sup>, Lyndon Despard Estes<sup>a</sup>

<sup>a</sup> Graduate School of Geography, Clark University, Worcester, MA, USA

<sup>b</sup> Environmental Studies Department, Carleton College, Northfield, MN, USA

<sup>c</sup> The Nelson Mandela African Institution of Science and Technology, Arusha, Tanzania

## ARTICLE INFO

### Keywords:

Land cover classification  
U-Net  
Random Forest  
African savanna  
PlanetScope  
Sentinel-1

## ABSTRACT

Accurate and timely land cover products are critical inputs for landscape planning, and provide key information for biodiversity conservation and food security. However, poor mapping quality and low resolution are considerable issues in existing land cover maps over the African savanna, where land use is complex and changing rapidly, and necessary ground-truth data are sparse and hard to obtain. To overcome this problem, to make optimal use of existing maps, and to minimize manual training data collection, we developed a three-stage ensemble method to make land cover maps. In the first stage, we extracted the consensus of multiple existing land cover products to generate fragmented pixel-wise training labels. In the second stage, we translated pixel-wise training labels to image-wise labels using Random Forest (RF) as a “gap-filling model”, with temporal features extracted from Sentinel-1 time series, raw bands, and vegetation indices derived from PlanetScope basemaps. These image-wise labels were scored and edited by humans and the quality information was used in the next stage. For stage three, we trained a U-Net network based upon these image-wise labels, using Sentinel-1 time series and raw bands of PlanetScope basemaps as image features. Using the information on label quality, a quality-weighted loss function was used in the network to reduce the impact of noise in the training labels. Using Northern Tanzania as a case study, the results demonstrate that ensembles of existing land cover maps provide a useful source of data for developing improved land cover maps over hard-to-classify, data-sparse landscapes. The Random Forest “gap-filling model” had an overall accuracy of 80.26% on our independent test dataset with 7 classes. The final U-Net model had an overall accuracy of 83.57%. This approach can be readily applied to other regions and extents (e.g., regional, global) and other data sources (e.g., Sentinel-2).

## 1. Introduction

Timely and accurate land cover maps covering large extents are critical for many environmental applications, such as natural resources management, biodiversity conservation, and food security assessment (Anderson et al., 2017; Jin et al., 2019; Leite-Filho et al., 2021; Pettorelli et al., 2016; Song et al., 2018). However, current land cover maps are often inadequate for agricultural and ecological applications due to their limited spatial and temporal coverage and low accuracy (Gómez et al., 2016), particularly over data-sparse regions, such as Africa savanna. In the past two decades, satellite imagery with high spatial and temporal resolution has steadily opened new avenues for timely mapping of land cover over large areas (Cheng et al., 2020; Tong et al., 2020). Meanwhile, rapid improvements in machine learning techniques have led to

dramatic gains in the accuracy of land cover classification (Campos-Taberner et al., 2020). Nevertheless, despite these gains, land cover mapping is still a major challenge in Africa's complex savanna landscapes with varying degrees of vegetation cover in space and time (Solbrig, 1996). One possible reason is the technical challenge of separating the woody and herbaceous components (Whitley et al., 2017). For these areas, the available global land cover products (Buchhorn et al., 2020a, 2020b; Congalton et al., 2017; Xu et al., 2019) that have high error rates when applied at regional scales, and perform poorly in savanna environments. Furthermore, existing savanna monitoring studies generally use coarse to medium resolution imagery that do not effectively represent fine grained components, such as nonforest trees (Abdi et al., 2022) and fields in smallholder agricultural systems (Jin et al., 2019; Kerner et al., 2020).

\* Corresponding author.

E-mail address: [lsong@clarku.edu](mailto:lsong@clarku.edu) (L. Song).

<https://doi.org/10.1016/j.jag.2022.103152>

Received 18 August 2022; Received in revised form 5 December 2022; Accepted 9 December 2022

Available online 12 December 2022

1569-8432/© 2022 The Authors. Published by Elsevier B.V. This is an open access article under the CC BY license (<http://creativecommons.org/licenses/by/4.0/>).

This latter problem of image resolution is being increasingly overcome by the mission of new satellites. Since late 2017, PlanetScope sensors started to supply near-daily satellite imagery with 3.7 m spatial resolution, which increases the possibility of obtaining clear observations during the rainy season (Planet Team, 2017; Roy et al., 2021). One of the higher-level derived products from this daily imagery are surface reflectance basemaps, which provide monthly to biannual composites of daily imagery in an analysis-ready format, substantially reducing the amount of pre-processing work (Estes et al., 2022) that must be undertaken to develop cloud-free mosaics. The recent Norway International Climate and Forests Initiative Imagery Program (NICFI) makes basemaps collected over tropical regions free to the public for sustainability-focused, non-commercial research (Norway's International Climate and Forest Initiative (NICFI), 2020), which is a game-changer for tropical land cover and land use monitoring. The availability of Sentinel-1 imagery also improves savanna monitoring because it is not affected by cloud cover (Torres et al., 2012) that frequently obstructs optical sensors over much of the tropical savanna biome (Roy et al., 2021). Given the recent release of the NICFI dataset, there are still relatively few studies that have applied these data for large area land cover mapping, particularly in combination with Sentinel-1 data (Vizzari, 2022). Existing applications of NICFI basemaps typically help visual image interpretation (Pascual et al., 2022; Rienow et al., 2022; Sugimoto et al., 2022) or evaluate the effectiveness of this dataset for delineating land cover (Aquino et al., 2022; Awuah and Aplin, 2021; Vizzari, 2022) within relatively small areas ( $<100,000 \text{ km}^2$ ), although efforts at larger sub-national (e.g. cropland mapping, Rufin et al., 2022) to continental extents are beginning to emerge (e.g. tree cover mapping; Reiner et al., 2022).

Alongside the newly available sources of high-frequency, high-resolution satellite imagery, there have been corresponding increases in the computational power needed to process large datasets, while advances in deep learning (DL) models have led to dramatic improvements in land cover mapping. The models based on the fully convolutional network (FCN) are among the most widely used deep learning architectures for land cover mapping (Chamorro Martinez et al., 2021; Solórzano et al., 2021; Volpi and Tuia, 2016) because they can achieve pixel-wise segmentation (Long et al., 2015).

A key obstacle to the wider adoption of these models for land cover mapping is the need to collect large, task-specific training and reference datasets. Despite recent investments in developing global ground truth datasets, which include observations within tropical savannas (Burke and Lobell, 2017; Laso Bayas et al., 2017; Schmitt et al., 2019), as well as new strategies to extend training samples (e.g., transfer learning and data augmentation; Shorten and Khoshgoftaar, 2019; Torrey and Shavlik, 2010), the available data are typically insufficient for training deep learning models over large areas. Since collecting labelled training data is time and labor-intensive, a more efficient labeling strategy is needed to meet the need for timely high-resolution land use/land cover products in these data-sparse but highly dynamic landscapes.

To overcome the challenge of developing the large label datasets that are needed to train deep learning models that can improve the ability to map savannas environments, our study had two primary objectives. The first was to develop a more automated and objective approach for generating labels that minimized the amount of manual effort. The second was to design a modeling approach that can account for and minimize the impact of label error (following Elmes et al., 2020).

To satisfy the first objective, we developed a technique for creating synthetic labels, in which several existing land cover products (Buchhorn et al., 2020a, 2020b; Congalton et al., 2017; Xu et al., 2019) were combined into a consensus land cover map, providing an initial set of labels that were more reliable than any of the individual inputs (following the rationale of Fritz et al., 2011), but provided only partial coverage of the study region (areas lacking consensus were excluded). To fill the missing data in the resulting synthetic labels, we trained a Random Forest (RF; Breiman, 2001) model to fill the gaps in selected

tiles, with predictors based on temporal features extracted from Sentinel-1 time series, as well as the raw bands of the PlanetScope basemaps and additional derived vegetation indices. We then visually assessed and manually edited the resulting gap-filled labels, producing a final set of fully labelled tiles, along with a quantitative measure of label quality. To meet the second objective, we used the resulting tiles to train a U-Net land cover model using a label quality-weighted loss function to minimize the impacts of label error.

We then applied this model to map the complex savanna landscapes of a  $243,416 \text{ km}^2$  region in Northern Tanzania, in the process demonstrating an efficient, semi-automated approach for training a model capable of generating improved, high resolution land cover data in hard-to-map, data sparse environment.

## 2. Materials and methods

### 2.1. Study area

We applied our proposed method to northern Tanzania (Fig. 1). This region is ecologically complex, comprising more than 4 ecozones, where the climatic conditions, soil moisture, and farming systems are different (Fig. 1) (Sebastian, 2009). Remote-sensing-based mapping of savanna in East Africa is challenging because savanna is a heterogeneous landscape (Solbrig, 1996) with varying degrees of vegetation cover and spectral similarities among land cover types (Tsalyuk et al., 2017; Zhang et al., 2019). These characteristics make this area an ideal case study, as its complex land cover provides an important baseline for our method, and the environmental context means that there is an urgent need for accurate land cover maps.

### 2.2. Datasets

#### 2.2.1. Satellite imagery

In this study, we queried 543 quads of PlanetScope Tropical

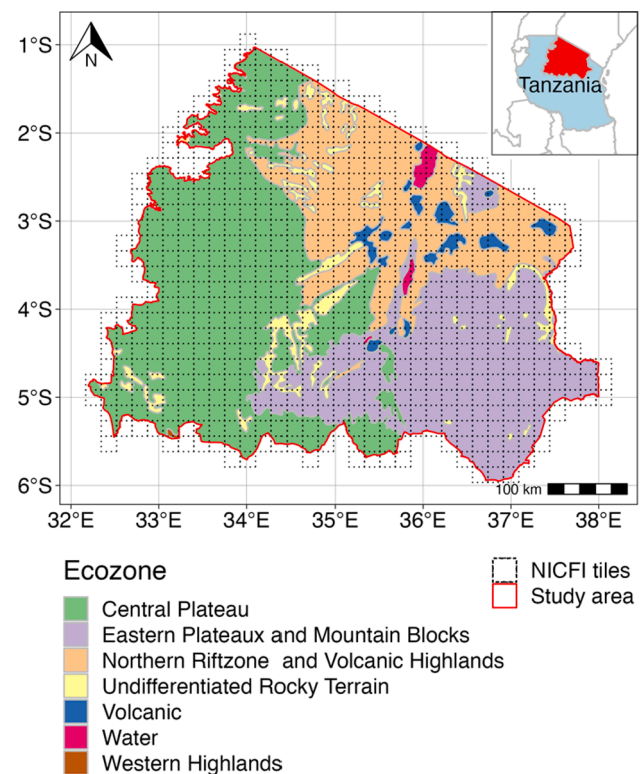


Fig. 1. The ecozones of the study area overlaid by the PlanetScope basemap tiling grid.



Normalized Analytic Biannual basemap from 2017 to 2018, which are provided by NICFI program. We collected imagery covering two seasons in each quad: December 2017–May 2018 (season 1), and June 2018–November 2018 (season 2). Having the spectral signature from multiple seasons helps to differentiate land cover types (Estes et al., 2022). To incorporate temporal features, we also used harmonic regression coefficients of Sentinel-1 time series (2017-10-01–2018-09-30). Harmonic regression coefficients summarize critical temporal features, enhancing the ability to differentiate land cover types based on seasonal information contained in the series (Moody and Johnson, 2001), while significantly reducing the number of raw images used. The coefficients were fitted on level-1 Ground Range Detected (GRD) Interferometric Wide Swath (IW) images acquired with dual polarization (VV + VH). Taking tile 1227–1002 as an example, Fig. 2 shows two seasonal NICFI basemaps, harmonic coefficients of Sentinel-1 dB in VV and VH polarization, and the spectral and temporal signature of land cover samples. The complete details of the images and image pre-processing can be found in Text S1 and S2 of the [supplementary material](#).

### 2.2.2. Pixel-level land cover (LC) reference labels

We developed an independent validation ( $n = 1286$ ) dataset to evaluate the quality of land cover products used in our study (Section

2.2.3), and to assess the performance of the land cover model. Two  $10\text{ m} \times 10\text{ m}$  squares in each quad within the study area were randomly selected, and hand-labeled by visual interpretation based on several virtual globe basemaps (e.g. Bing or Google Maps), satellite imagery in this study (Section 2.2.1), prior knowledge, and web searches of local landscape pictures. Despite the small size of the squares, they occasionally contained more than one class. In these cases, we shifted the squares so that they covered a single class.

### 2.2.3. Land cover (LC) products

To initialize the training dataset for our land cover mapping models (see Section 2.3), we prepared an ensemble of existing land cover products, which we turned into consensus labels. After pre-assessment (see Text S3), we selected 4 products to use (Table 1): Copernicus

**Table 1**

Land cover products used and their accuracies over the study region.

Product name	Product type	Year	Resolution	Overall accuracy
CGLS LC100m	Land cover	2018	100 m	67.70 %
FROM-GLC 2017v1	Land cover	2017	30 m	60.13 %
GFSAD30	Crop mask	2015	30 m	82.93 %
TanSIS	Crop mask	2018	250 m	82.39 %

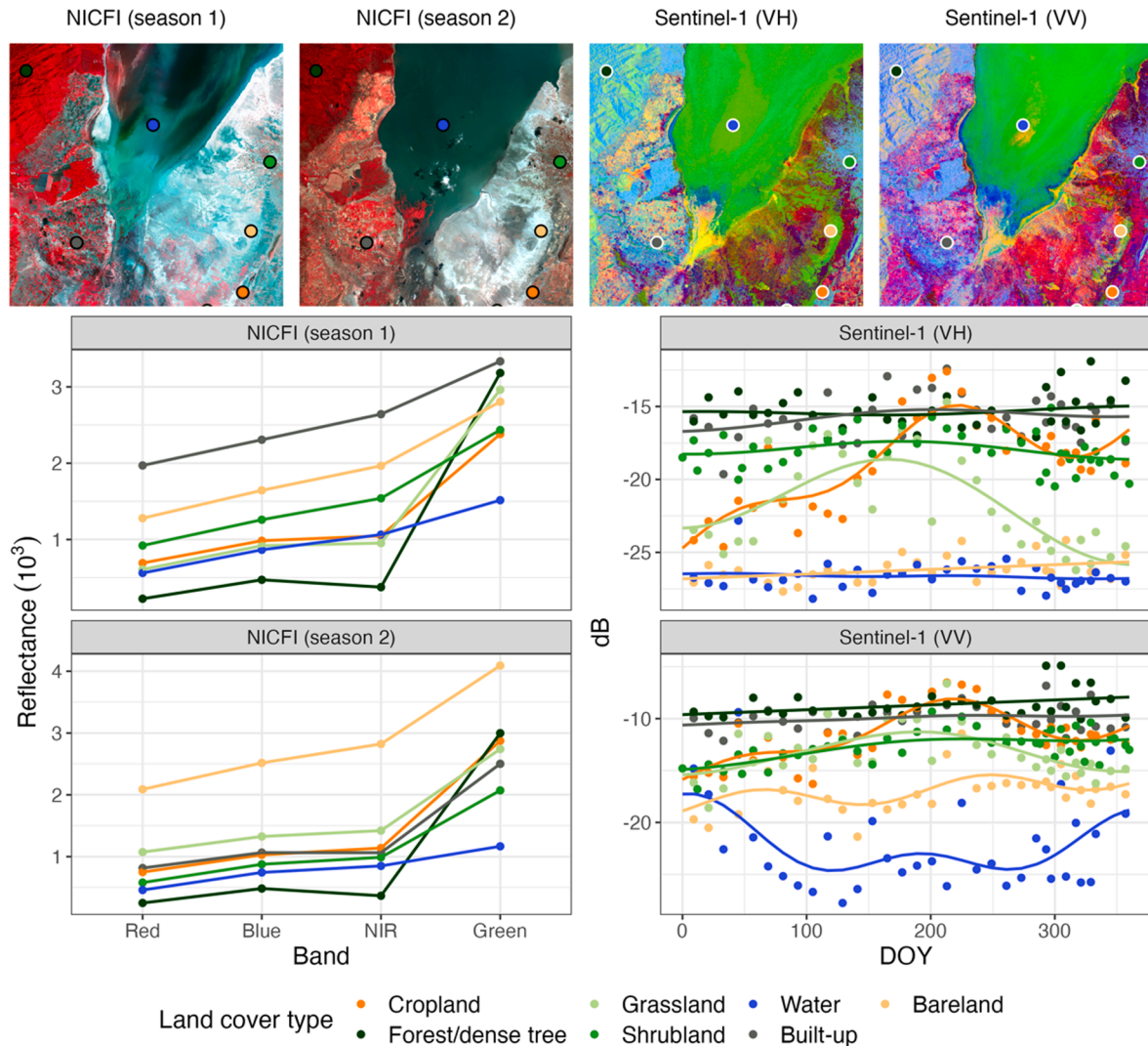


**Fig. 2.** Seasonal NICFI basemap in false-color, harmonic coefficients (RGB: Slope,  $\cos(\frac{2\pi t}{dt})$ , Intercept) of Sentinel-1 dB in VV and VH polarization, spectral signature, and temporal signature of land cover samples in an example tile (1227–1002).

global land cover map (CGLS LC) (Buchhorn et al., 2020b), Finer Resolution Observation and Monitoring – Global Land Cover (FROM-GLC) (Gong et al., 2019), Global Food Security-support Analysis Data (GFSAD) cropland extent of Africa (Congalton et al., 2017), and a cropland layer produced by the Tanzania Soil Information Service (TanSIS) (Walsh et al., 2018). CGLS LC has 23 classes according to UN-FAO's Land Cover Classification System (LCCS). FROM-GLC includes 10 main land cover classes. GFSAD and TanSIS are cropland masks, although GFSAD has an extra water class. Even though each product was separately validated, the quality of these products in our study area is unclear. We, therefore, used the independent validation dataset (Section 2.2.2) to evaluate their accuracies, which are listed in Table 1 (complete details of the assessment are in Table S2). Besides gridded LC products, OpenStreetMap (OSM) vector layers also were used as ancillary datasets in both generating consensus labels and land cover classification.

### 2.3. Modeling approach

The land cover mapping approach we developed has three main parts (Fig. 3). In the first part, we created an ensemble map from the selected land cover products (Section 2.2.3) as land cover reference labels. In the second part, we trained a pixel-based Random Forest model, selected a group of tiles, and used the model to fill the gaps between labelled fragments obtained in part 1 in these tiles, in order to make complete image-wise labels. A deep learning network was then trained using these gap-filled labels in the third part.

#### 2.3.1. Part 1: Ensemble multiple land cover (LC) products

Several previous studies have demonstrated the effectiveness of deriving training labels from existing land cover products (Ren et al., 2022; Yang and Huang, 2021; Zhang et al., 2021). We made consensus land cover labels from assembled land cover products (Table 1). These land cover products were made in different years based on varied features, therefore identifying where these products agree helps to increase confidence in the accuracy of the underlying land cover classification (Fritz et al., 2010; Pérez-Hoyos et al., 2020), while also providing information on how stable and how difficult a landscape is to classify. We assume that pixels where all maps agree represent stable landscapes, while the pixels in which maps disagree are either areas undergoing rapid changes (e.g., fallows) or those that are hard to distinguish from other cover types (e.g., degraded savannas versus croplands).

To create the ensembles, we aggregated the land cover types into 8 common classes that could be extracted from the different taxonomies of these land cover products, which were cropland, forest/dense tree, shrubland, grassland, water, wetland, built-up, and bareland (which in this region are typically degraded savannas) (Doggart et al., 2020). The

selected land cover products were either multi-class land cover products or binary cropland layers. Multi-class land cover maps were first reclassified into the same classes (Table S1), combined, and then the consensus areas were extracted from these layers. Because cropland is a difficult class to predict and thus was assigned poor quality consensus labels, a different strategy was applied to the cropland class. GFSAD30 and TanSIS were combined together to mask out cropland areas to make consensus labels of other classes. GFSAD30 was then used singly as the cropland label at this stage due to its higher spatial resolution and classification accuracy.

The resulting consensus labels still contained significant noise because the input maps were derived from low to moderate spatial resolution imagery (Table 1). These errors were mainly concentrated along the boundaries of different cover types, such as roads, rivers, and built-up regions. To reduce the impact of boundary uncertainties, we used buffered OSM layers, including roads, rivers, and buildings, to mask out such areas. This process resulted in a set of consensus land cover labels that were highly fragmented (Fig. 4A) and were thus not optimal for training fully convolutional neural networks, for which image-based training labels are optimal for providing the model with spatial context.

#### 2.3.2. Part 2: Creating gap-filled land cover labels

To convert the fragmented consensus labels into image-wise labels (Fig. 4B) suitable for training a U-Net, we trained a pixel-based Random Forest (Breiman, 2001) model using a random sample of consensus LC labels. As the moderate-resolution land cover maps miss many small inland waterbodies and have low location precision in settlements, we removed waterbodies and built-up areas from the consensus labels and instead sampled labels for these two classes from the OSM layers. We did not explicitly model wetlands, because they constitute a very rare class without unique features in our study area. To develop the model, we analyzed variable importance and selected the best hyper-parameters (see details in Fig. S4). The model was trained using the 4 bands of semi-annual NICFI basemaps, and the harmonic regression coefficients extracted from both polarizations of the Sentinel-1 time series (see Section 2.2.1). Additional features included the normalized difference vegetation index (NDVI), soil-adjusted vegetation index (SAVI), two-band enhanced vegetation index (EVI), and atmospherically resistant vegetation index (ARVI) (Huete, 1988; Jiang et al., 2008; Jin et al., 2019; Kaufman and Tanre, 1992; Tucker, 1979) calculated from each basemap pair. To minimize the computation costs of training the neural network, we split the original quad size of  $4096 \times 4096$  pixels into  $8 \times 8$  sub tiles of  $512 \times 512$  pixels (Fig. 4). After training the gap-filling model, 4 sub tiles within each quad were randomly selected to generate predicted labels, with 3 labels reserved for training the neural network, and one reserved for validation.

The resulting gap-filled land cover labels were imperfect (see Fig. 4B), therefore in a second step, we manually checked and edited labels where needed. Final label quality was assessed against two dimensions: the correctness of the label after editing and the difficulty of the tile to be classified. The correctness of the label was assessed based on visual interpretation of the underlying land cover in the basemap imagery, while the difficulty of labeling was graded based on how many edits were made to the predicted label tile, with more edits indicating increasing difficulty. Both measures were graded from low (1) to high (5). We refer to the resulting scored and edited labels as human refined labels (Fig. 4C), which, along with their quality information, were used to train the neural network.

#### 2.3.3. Part 3: Land cover classification with U-Net

We applied a widely used deep learning architecture, U-Net (Text S4 and Fig. S2), to train the image-based land cover model. Compared to more complex architectures (e.g., Deeplab), U-Net requires fewer training samples and achieves good performance with a substantially lower computational cost (Ronneberger et al., 2015). Thus, U-Net is a

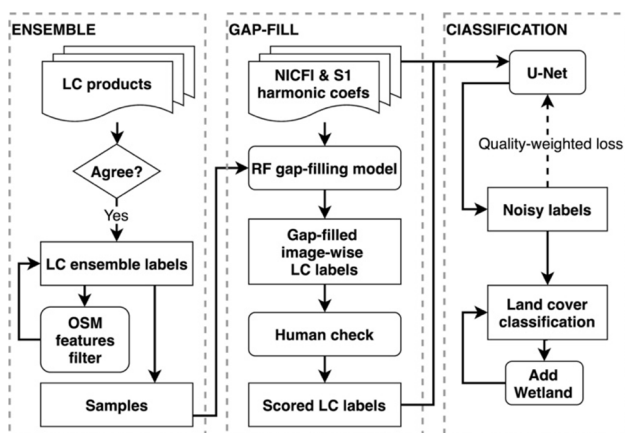
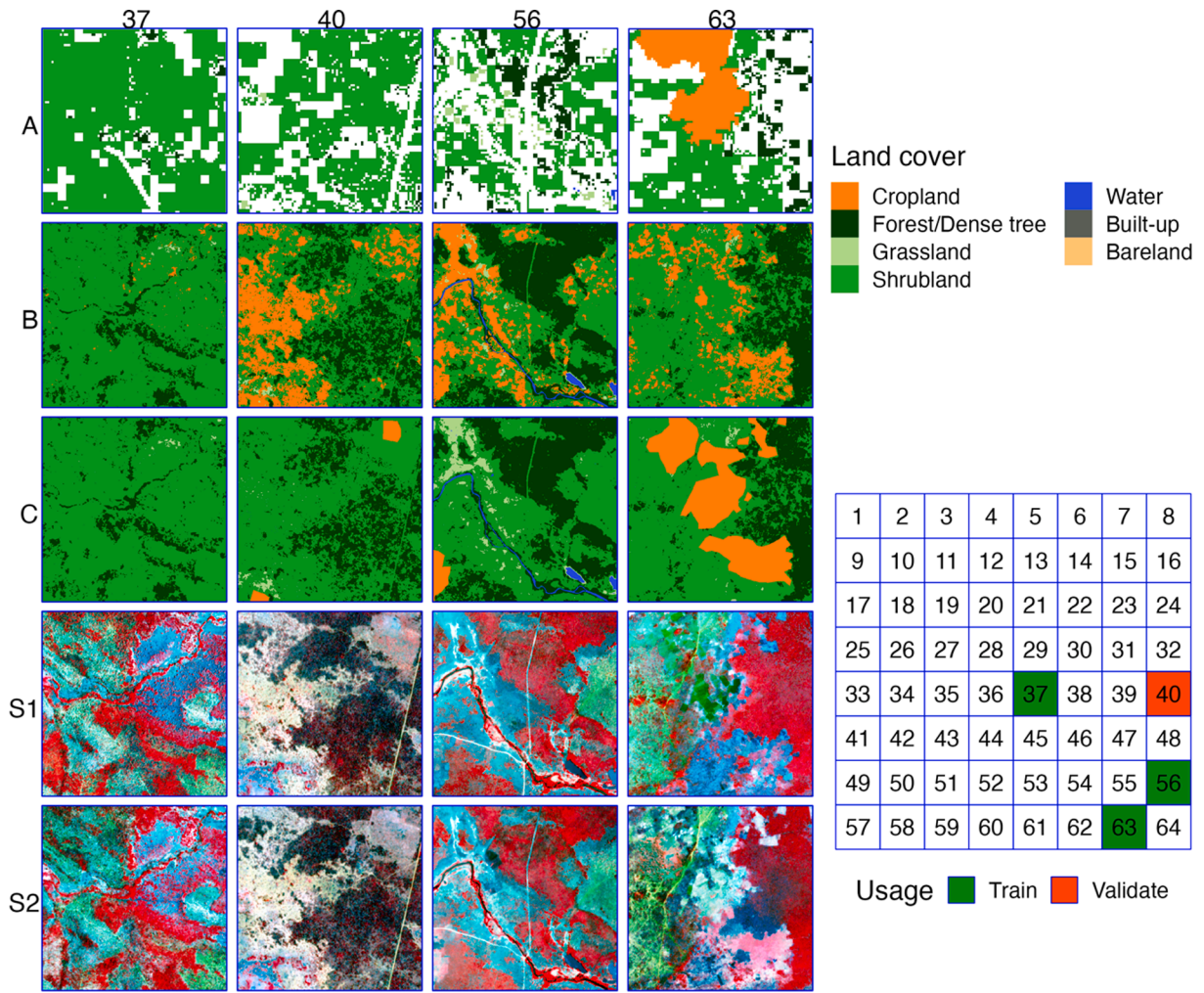


Fig. 3. The workflow of the proposed approach (OSM stands for OpenStreetMap).





**Fig. 4.** Sub-tiling system and different types of label examples (A are the weak ensemble labels, B are the gap-filled labels produced by a Random Forests model, C are the human refined labels, and S1 and S2 are false-color composites of PlanetScope NICFI basemaps in season 1 and season 2).

popular method for land cover classification, particularly when training examples are limited (Rakhlin et al., 2018).

Optimization algorithms play an important role in training a deep neural network (Sun, 2020). A good optimizer enables the network to obtain the optimal weight matrix efficiently. In this study, we selected a recently proposed combined optimization method (AdaBound) that works like adaptive methods at the early stage of training to get fast training speeds, then smoothly transforms to Stochastic Gradient Descent (SGD) at the end to attain good overall generalization and model performance (Luo et al., 2019).

The learning rate for gradient descent is also critical in neural network training that impacts the model's ability to converge on a solution (Bengio, 2012). In this paper, we applied a combined learning rate scheduler that included multiple constant and cyclical learning rates (Smith, 2017) for all experiments.

In a convolutional neural network, data augmentations, such as scale and rotation, are effective strategies to increase the variance of training data and improve the generalizability of the network (Perez and Wang, 2017; Shorten and Khoshgoftaar, 2019). At training time, we randomly flipped the original images horizontally or vertically. Diverse imaging conditions of CubeSats lead to photographic variations in scale and changes of illumination in PlanetScope imagery (Houborg and McCabe, 2018). These variations effectively mimic the brightness shift that is typically used for data augmentation; therefore, we did not implement this particular augmentation strategy. We did not employ rotations or stretching because they may alter image-level labels or break the spatial

symmetry.

To reduce the impact of class imbalance and noisy labels, we weighted loss by class frequency as well as the quality of labels in each training image (Eq. (1)). The dimensions of the input for the loss function were  $(B, C, H, W)$ , where  $B$  is the number of images in each mini-batch,  $C$  is the number of classes,  $H$  is the height of the image, and  $W$  is the width of the image.  $N$  is the overall number of pixels, which equals  $B \times H \times W$ .

$$loss(x, y) = \frac{\sum_{b=1}^B l_b \times w_{cb} \times w_{db}}{\sum_{n=1}^N w_{yn} \bullet 1\{y_n \neq index_{ignore}\}} \quad (1)$$

$l_b$  is the sum of class-balanced cross entropy loss per pixel in an image, then:

$$l_b = \sum_{h=1}^H \sum_{w=1}^W -w_{y_{hw}} \log \frac{\exp(x_{hw, y_{hw}})}{\sum_{c=1}^C \exp(x_{hw, c})} \bullet 1\{y_{hw} \neq index_{ignore}\} \quad (2)$$

where  $x$  is the input,  $y$  is the target,  $w$  is the class-balanced weight,  $w_c$  is the normalized weight of label correctness, and  $w_d$  is the normalized weight of label difficulty.

The original measure of label correctness  $c$  ranges from 1 (least correct) to 5 (most correct), which are then normalized to weights (0–1) using a logistic function  $w_c = \frac{1}{1+e^{-k(c-c_m)}}$ , where  $k$  is the growth rate and  $c_m$  is the  $c$  value of the midpoint. In  $w_c$ , we only changed  $k$  and used the constant value 2.5 for  $c_m$ , which is the median of original correctness values. The original value for labeling difficulty  $d$  ranges from 1 to 5

(least to most difficult), which are rescaled to a user defined range  $[1, s_{max}]$  as weights using equation  $w_d = \frac{(s_{max}-1) \times (d-d_{min})}{(d_{max}-d_{min})} + 1$ . The rescaling functions are flexible to be designed in any forms (e.g., linear) based on different modeling demands. We picked these functions based on their regularization ability and the quality condition of the labels in this project.

The correctness weight reduces the contribution of images with poor label quality to the calculation of the loss function, thereby decreasing the risk that the network learns incorrect information from noisy labels. In contrast to correctness weights, the role of difficulty weights is to force the model to pay more attention to images that are hard to classify, which helps improve the generalizability of the model to other areas or time intervals. However, difficulty weights that are too high may cause the network to overfit on difficult labels, therefore we recommend smaller values of  $s_{max}$ , generally from 1 to 1.2. An analysis of weight parameters of quality-weighted and class-balanced loss was given in Text S6 of [supplementary materials](#). In our study, when growth rate  $k$  of the logistic function used to calculate the correctness weight ( $w_c$ ) is set to 1.5, the best performance ( $AA = 0.880 \pm 0.002$ ) was achieved (Fig. S3). The values of  $s_{max}$ , used to calculate the difficulty weight ( $w_d$ ), from 1 to 1.1 were reasonable choices for this study (Text S6 and Fig. S3).

## 2.4. Accuracy assessment

To assess the LC products and modeling results, we used the true negative rate (TNR, also called specificity), negative predictive value (NPV), user's accuracy (UA, also called consumer's accuracy, precision, or positive predictive value), producer's accuracy (PA, also called recall, true positive rate or sensitivity), balanced accuracy (BA), and the F1 score (Barsi et al., 2018; Brodersen et al., 2010; Elmes et al., 2020; Olofsson et al., 2014). For U-Net training, we also used intersection over union (IoU) and the average (mIoU). The calculation details for these metrics are provided in Text S5 of [supplementary materials](#).

## 3. Results

### 3.1. Land cover label gap-filling

The Random Forests label gap-filling model (number of trees: 1000, number of independent variables: 28, mtry: 11) was trained with  $1.24 \times 10^6$  samples randomly selected from the ensembled land cover products (roughly 48 % of the area). Twenty percent of the samples were used for hyper-parameter tuning with a grid search and model validation (Table 2). The independent reference dataset (Section 2.2.2) was used to assess model performance (Table 2).

The model selection process showed that radar backscatter (Fig. S4) was an important feature for land cover classification, with variables representing harmonic regression coefficients describing one intra-annual seasonal cycle being much more influential in distinguishing land cover types than those characterizing two seasonal cycles, while the coefficient of  $\cos\left(\frac{2\pi t}{d_{yr}}\right)$  was more important than  $\sin\left(\frac{2\pi t}{d_{yr}}\right)$ , which is also

evident in Fig. 2. Optical images captured in the growing season were more influential than those from the off-season (Fig. 2), while among the spectral features, NIR and vegetation indices contributed more than the visible bands. The trained Random Forest had an overall accuracy of 80.26 % and an average F1 of 76.85 %, but with substantial performance differences across different land cover types (Table 2 and Fig. S5).

The resulting gap-filled models produced a set of 2,572 image-wise labels that were generated purely by machine intelligence, which were then improved using human supervision. Each label was manually checked and refined as needed, requiring an average of 0.8 min per label and a total estimated effort of 34 h (see Table S3 in the [supplementary material](#) for further details on effort). Many (39 %) labels had good quality and did not need editing, and thus had high correctness and low difficulty scores (Fig. 5). In all, 61 % of the labels were edited, with the majority of these (85 %) needing only minor editing (difficulty score of 1–2), while the remaining 15 % needed moderate to extensive editing (difficulties of 3–5). A small quantity (6 %) of labels had correctness scores lower than five because these were too complex to be edited. The resulting human-refined, image-wise labels and their quality information were used to train the U-Net land cover segmentation model.

### 3.2. Land cover classification with U-Net

To train the model, we used original spectral bands of two seasonal NICFI images and intercept, slope, and coefficient of  $\cos\left(\frac{2\pi t}{d_{yr}}\right)$  of Sentinel-1 time series as input channels of U-Net, which were selected based on their variable importance values for Random Forests (Section 3.1 and

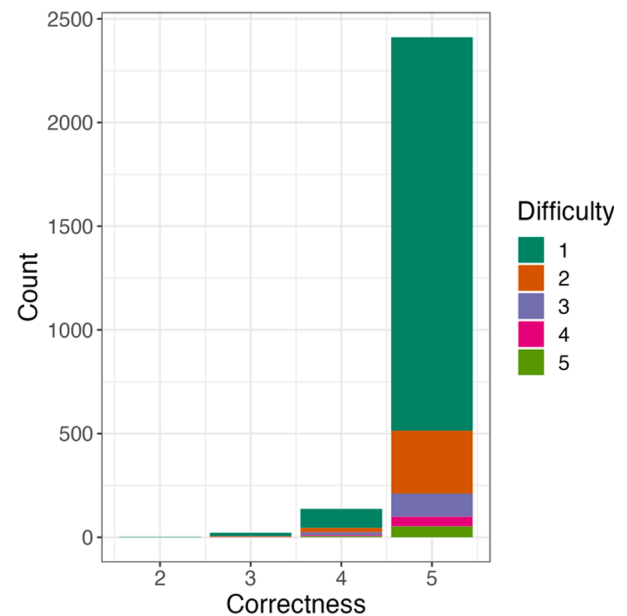


Fig. 5. Distribution of human refined label quality.

Table 2

The evaluation of the random forest gap-filling model.

Class	Validation PA	Independent test (overall accuracy: 80.26 %)					
		TNR	NPV	UA	PA	BA	F1 score
Cropland	84.24 %	88.17 %	96.21 %	80.05 %	93.18 %	90.67 %	86.12 %
Forest/Dense tree	95.04 %	98.23 %	98.56 %	64.23 %	69.02 %	83.62 %	66.54 %
Grassland	87.52 %	93.30 %	94.99 %	69.06 %	75.26 %	84.28 %	72.03 %
Shrubland	86.06 %	94.47 %	85.62 %	88.28 %	72.43 %	83.45 %	79.57 %
Water	96.74 %	99.57 %	99.93 %	89.14 %	98.01 %	98.79 %	93.36 %
Built-up	73.62 %	99.46 %	98.77 %	83.70 %	69.06 %	84.26 %	75.68 %
Bareland	96.78 %	99.82 %	99.35 %	81.13 %	53.75 %	76.79 %	64.66 %
Average	88.57 %	96.14 %	96.21 %	79.37 %	75.82 %	85.98 %	76.85 %

Fig. S4). Other inputs were not used in order to minimize computational demand. For the learning rate scheduler, we selected values that ranged from 0.001 in earlier epochs to 0.0001 in the final epochs (Fig. 6A). The selected validation sub tiles (Section 2.3.2 and Fig. 4) were used for model tuning and model validation, and the independent reference dataset (Section 2.2.2) was also used for final model testing (Table 3). The computational environments are described in Text S4 in the supplementary material.

The model training curves (Fig. 6) showed that the U-Net model achieved relatively high accuracy for almost every class after just a few epochs (10–25), with gradual improvement thereafter with fluctuations in the curve becoming more stable in later epochs. The mIoU curve reveals that the model was less effective in achieving shape accuracy than overall accuracy, given the slower rate of improvement and significant fluctuations. The learning curves for the cropland and built-up classes showed a characteristic pattern of rapid but steady growth until reaching a plateau, with high values for each class achieved on the independent accuracy assessment (92–97 %, Table 3) test. In contrast, the training curves for the forest/dense tree and bareland classes rapidly jumped to a plateau, with larger fluctuations evident in the forest class.

This likely reflects the same tendency to over-fit these two classes that were evident in the Random Forest gap-filling model (Section 3.1). The same behavior is also evident in the learning curve for water, but in this case, the model is able to effectively generalize for this class (98–99 % accuracy; Table 3) because of its relatively unique and globally consistent spectral characteristics. Grassland and shrubland had learning curve progressions similar to those of the cropland and built-up classes, but with substantial fluctuations. These two types were more confusing for the network, given their spectral similarity with each other and with croplands.

The U-Net model achieved an overall accuracy of 83.57 % and an average F1 of 81.66 % on our independent test dataset. The average balanced accuracy across classes was 91.77 % (range 84.89–98.53 %), with average producer's accuracy (PA) of 86.57 % (range 76.29–98.01 %) and average user's accuracy (UA) of 78.32 % (range 50.26–98.17 %). Forest/dense trees had a high commission error (UA = 50.26 %) and were often classified in places that were in fact shrublands (Fig. 7), while also having a high commission error (UA = 87.07 %) as it was often confused with grassland (Fig. 7). Besides forests/dense trees, grassland and shrubland were the two hardest classes for U-Net to learn, particularly shrubland, which has diverse features that are easily confused with croplands, forests, and grasslands (Fig. 7).

Besides the land cover map, U-Net also produced a map of classification confidence (Fig. 8) with values ranging from 18 to 99 to provide a reference for downstream studies such as yield estimation or land cover change analysis, following recommendations by Elmes et al (2020). The classification confidence is the pixel-wise maximum value of class probabilities produced by softmax after U-Net (Fig. S2). Over the whole study area, the cropland, forest/dense trees, grassland, shrubland, and bareland classes had fairly similar average confidence scores (80–84 %; Table 3), while water had the highest mean score (94.89 %; Table 3) and built-up the lowest (70.11 %; Table 3). It is noteworthy that there was some noise in the predicted water class due to dark objects in the original images, such as shadows.

### 3.3. Final land cover map

After completing the final land cover classification, we added the wetland class by rasterizing the OSM layer (Fig. 9A). Because the wetland class was not calculated by U-Net, we did not assign this class

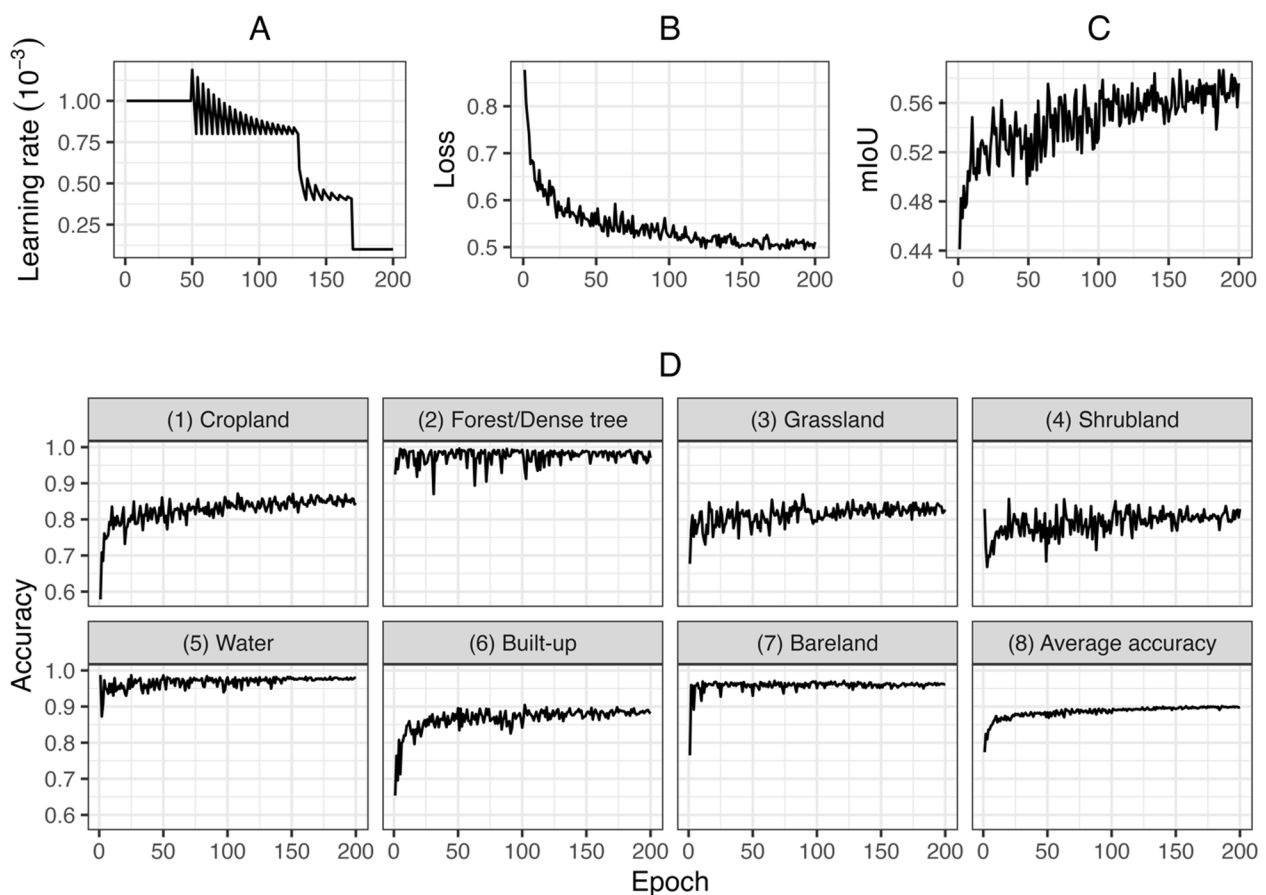


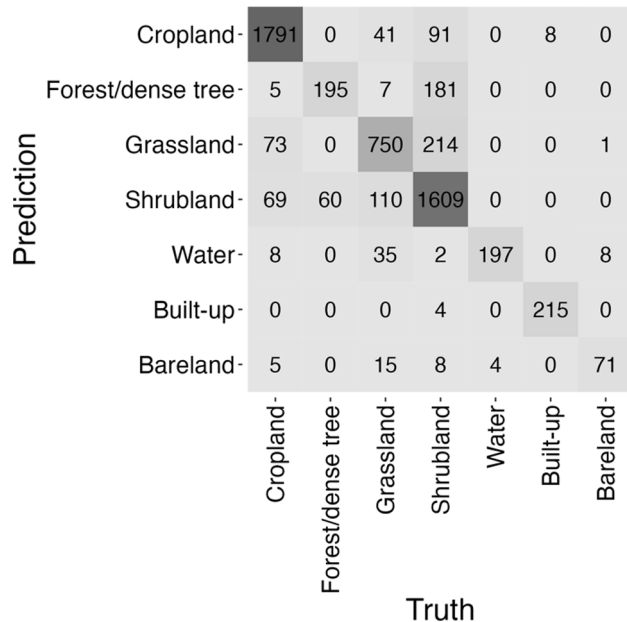
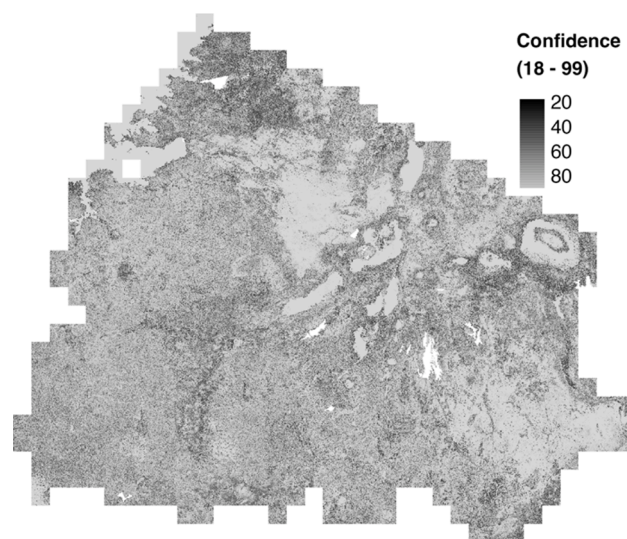
Fig. 6. Evolution of the learning rate (A), loss function (B), mean IOU (C), accuracy of each class (D1–D7), and average accuracy (D8)) on the validation dataset during model training.



**Table 3**

Validation, independent test accuracy and prediction confidence of U-Net model.

Class	Validation PA <sup>1</sup>	Independent test (overall accuracy: 83.57 %)						Prediction confidence (95 % interval)
		TNR	NPV	UA	PA	BA	F1 score	
Cropland	85.20 ± 0.78 %	96.34 %	95.84 %	92.75 %	91.80 %	94.07 %	92.27 %	81.27 ± 15.10 %
Forest/Dense tree	97.47 ± 1.14 %	96.50 %	98.89 %	50.26 %	76.47 %	86.49 %	60.65 %	83.95 ± 17.48 %
Grassland	83.03 ± 1.02 %	94.02 %	95.61 %	72.25 %	78.29 %	86.16 %	75.15 %	82.82 ± 17.12 %
Shrubland	80.91 ± 1.47 %	93.48 %	87.27 %	87.07 %	76.29 %	84.89 %	81.32 %	82.56 ± 16.68 %
Water	97.73 ± 0.20 %	99.05 %	99.93 %	78.80 %	98.01 %	98.53 %	87.36 %	94.89 ± 12.18 %
Built-up	88.51 ± 0.35 %	99.93 %	99.86 %	98.17 %	96.41 %	98.17 %	97.29 %	70.11 ± 18.41 %
Bareland	96.22 ± 0.19 %	99.44 %	99.84 %	68.93 %	88.75 %	94.09 %	77.60 %	79.93 ± 18.62 %
Average	89.87 ± 0.10 %	96.97 %	96.75 %	78.32 %	86.57 %	91.77 %	81.66 %	82.43 ± 16.53 %

<sup>1</sup> Average PA of last 10 epochs.**Fig. 7.** Confusion matrix heatmap of the independent test of U-Net classification model.**Fig. 8.** The confidence map of land cover classification by U-Net.

any confidence value (Fig. 8). Reasonably, the U-Net model has higher confidence over homogeneous areas, such as water bodies, grassland in the north, and shrubland in the southeast (Fig. 8). The model has low confidence over the northwest area (Fig. 8), where it is a complex mixture of cultivated crops, tree crops, built-up, and native vegetation. Similar performance was attained over the foothills and hillside of Mount Kilimanjaro, where people are growing cultivated crops and coffee mixing with native vegetation.

In northern Tanzania, the predominant land cover types are cropland, shrubland, and grassland (Fig. 9B & 9C). The error-adjusted area estimate (Olofsson et al., 2014) with a 95 % confidence interval of the cropland is  $86755 \pm 1438.3 \text{ km}^2$ ; shrubland is  $83940.3 \pm 1985.6 \text{ km}^2$  and grassland is  $43811.4 \pm 1734.7 \text{ km}^2$ . Most of the cropland is distributed in the Central plateau agro-ecological zone, with plains and arable lands (Figs. 1 & 9A). The southern part of this zone is less cultivated and is largely covered by shrubs. Shrubland are found primarily in the Eastern plateau zone with a moist climate, where the land is mainly uncultivated because it is falls within protected areas. Grasslands predominate in the Northern riftzone and volcanic highlands, where the Serengeti National Park, Ngorongoro Conservation Area, and Arusha National Park are located.

Comparisons of our land cover maps within different agro-ecological zones with the two existing multi-class land cover products used to make consensus labels show that our predictions inherited the advantages and mitigated the errors contained within the original land cover products. For example, Fig. 10a shows that our model reduced the substantial omission error in built-up areas and shrubland in the other two products while maintaining the broad distribution of croplands, and Fig. 10b shows that our updated map more effectively captures forests and croplands. Fig. 10c shows that CGLS\_LC overestimated cropland while FROM-GLC overestimated shrubs, and our prediction reduced these issues significantly. Similarly, in Fig. 10d, CGLS\_LC underestimated cropland and our prediction detected cropland as effectively as FROM-GLC. Owing to the high resolution of satellite imagery, our predictions reveal more landscape details and delineate more precise object boundaries. For instance, the dense tree cover within riverine forests is clearly delineated (Fig. 10c), as well as scattered residential areas (Fig. 10a).

#### 4. Discussion

Our results demonstrate an effective and operationalizable approach for mapping land cover in data sparse areas, which is capable of producing greatly improved land cover data in hard to map tropical savannas, where up-to-date and accurate land change information is critical given the rapid pace of change (Bullock et al., 2021) and the relative inaccuracy and infrequent production of existing land cover products. The resulting map has noticeable improvements in land cover type differentiation relative to existing land cover products, particularly in cropland and grassland. These gains are in part attributable to the integration of high-resolution PlanetScope NICFI basemaps, which significantly enhances object boundary delineation, and improves



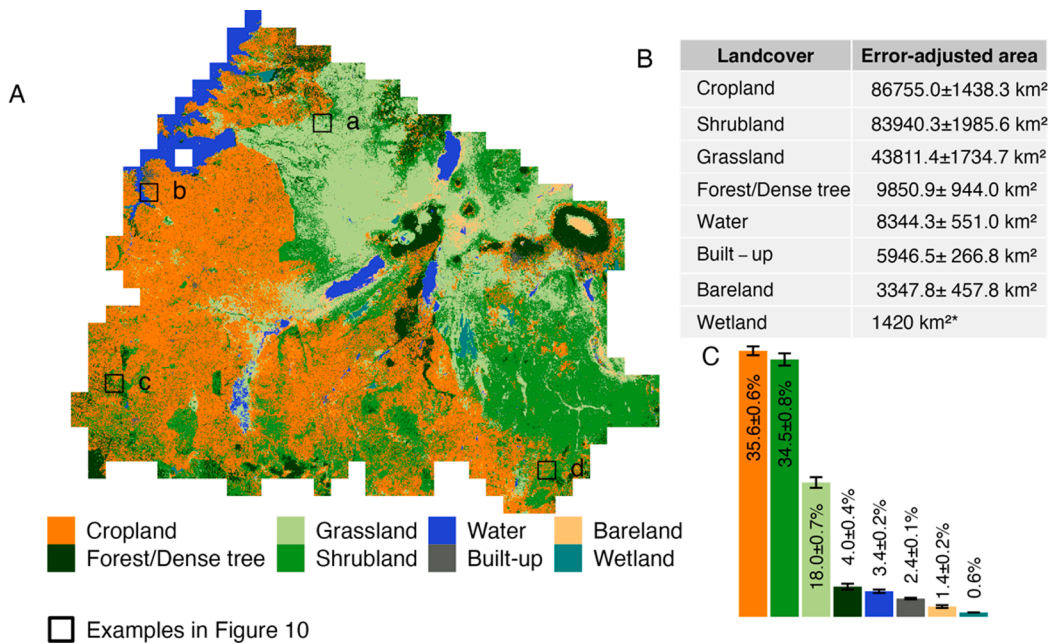


**Fig. 9.** Predicted land cover (A), error-adjusted area estimates (B), and proportion of each land cover type (C) with 95% confidence interval over the study area (\*The estimated area of wetland is directly calculated by the rasterized OSM layer without error adjustment).

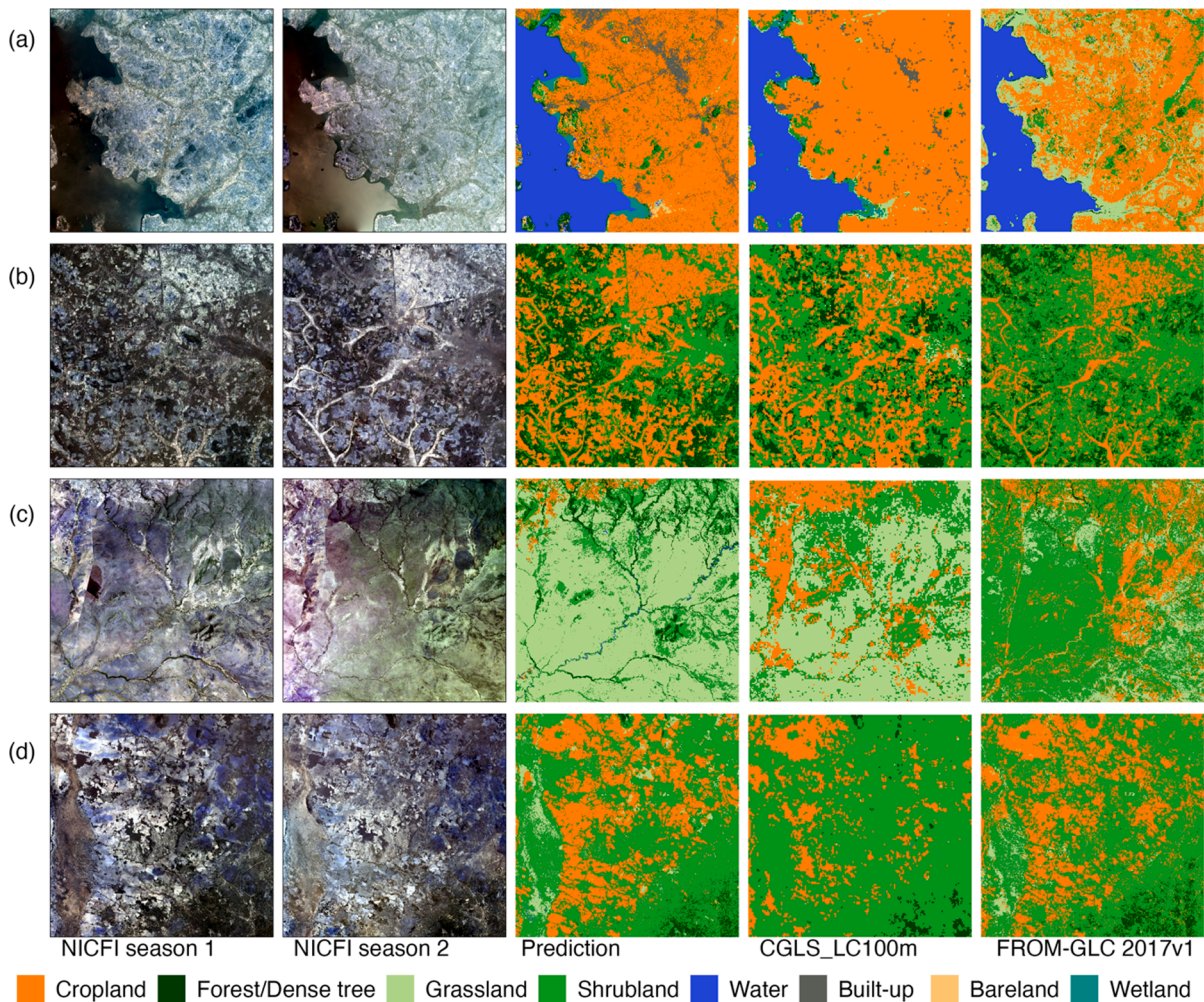


**Fig. 10.** Seasonal NICFI images, prediction in this study, and the CGLS\_LC100m and FROM-GLC 2017v1 product of four example tiles (a and b are in Central plateau agro-ecological zone, c is in Northern Riftzone and Volcanic highlands zone, and d is in Eastern plateau zone).

detection of minor land cover types (e.g., residential) and the description of landscape patches. The Sentinel-1 time series provides a cloud-free temporal signature of landscape features, which can overcome the spectral limitations of optical satellite imagery (e.g., PlanetScope) and increase the ability to distinguish different land cover types (Jacob et al., 2020).

A key feature of our approach that enables its operationalization is its ability to generate a large number of labels without intensive human effort, which it does by leveraging existing land cover datasets. Even though these data individually have substantial problems and often perform poorly in our study area (Table S2), particularly because they are developed over regional to global extents (Buchhorn et al., 2020b; Congalton et al., 2017; Gong et al., 2019; Walsh et al., 2018), using the consensus of these products can provide a useful starting point for collecting a large number of training samples that can be synthetically improved through an easily implemented machine learning approach. As a widely used algorithm, Random Forest performs well for land cover classification (Sheykhoumousa et al., 2020; Talukdar et al., 2020), has interpretable structure, and provides additional variable importance information that can be used to inform further modeling efforts. It can be trained using both point- and image-based training samples, which makes the model easy to rapidly develop and apply. However, the algorithm cannot learn from the spatial patterns of features or their relationships (Breiman, 2001; Chan and Paelinckx, 2008), thus it is necessary to carefully select additional supplementary features that can improve model performance. Neural network architectures, such as U-Net, which can learn from contextual patterns in imagery to improve object boundary delineation (Igloukov et al., 2017; Rakhlin et al., 2018), and thereby overcome one of Random Forest's major limitations. However, this improved performance comes at the expense of collecting larger volumes of training data, consisting of chips that are fully labelled to provide the model with the necessary spatial context. Even though strategies such as weak supervision (Wang et al., 2020) have been proposed to reduce labelling effort by using fragmented labels, the lack of precise localization information can lead to the failure of small size objects, particularly across complex fragmented landscapes. Using two models together as we have done here plays to each model's strengths while helping to overcome the major challenge of limited training data.

There, nevertheless, is still room for improvement in both approach and datasets. In our study, we simply resampled S1 SAR imagery to align with PlanetScope NICFI basemaps in order to make full use of the high resolution and reduce the risk of adding more uncertainties due to extra processing. In fact, multiple methods better than resampling exist to deal with imagery with different scales. The time intervals for semi-annual NICFI basemaps are not customized regionally, which may not match with local seasonality. In this study, we selected NICFI scenes (2017-12-01–2018-05-30 and 2018-06-01–2018-11-30) covering dates that generally align with the agriculture year (2017-10-01–2018-09-30). Because PlanetScope basemaps were mosaiced every-six months, we assumed a two-month shift would not cause any significant issues in dynamic landscapes. This deficiency, however, can limit the mapping ability that relies on temporal signatures in spectra (e.g., mapping crop types).

In the Sub-Saharan African landscape, fallow is a common and critical land-use type, but it is usually not a target class in coarse level land cover studies. The fallow is often interpreted as farmland due to its regular shape and close location to active farmland. However, it has more similar spectral and temporal features to grassland or bareland (Tong et al., 2020). This could be a significant reason for misclassification.

## 5. Conclusion

We provided an operational workflow for rapid land cover mapping that can be applied to heterogeneous landscapes without good ground truth references. The proposed workflow ensembles not only multiple LC

products but also artificial and human intelligence to increase classification reliability. We then demonstrated its capacity to map a complex tropical savanna landscape in Northern Tanzania. The resultant land cover map can be used in investigating agricultural expansion and development, analyzing deforestation or sustainability of protected areas, and many other ecological applications.

Additionally, we provided a high-resolution land cover dataset with label quality information at large scales across the savanna landscape. It well presents features, structures, and distribution of major land cover categories in our study area. Therefore, they can be used to train different types of land cover models, and more importantly to investigate how to improve land cover mapping with noisy labels that are inevitable in the real world. The pre-trained U-Net network upon this dataset can directly be used to map land cover if the landscape condition is similar and input datasets are available. It can also be fine-tuned and transferred to other cases or years.

The land-cover dataset and land cover map produced in our study are accessible under <https://osf.io/4qj36/>. Code of workflow and of pre-processing satellite image for this article can be found on GitHub at <https://github.com/LLeiSong/hrlcm> and <https://github.com/LLeiSong/sentinelPot>.

## CRedit authorship contribution statement

**Lei Song:** Conceptualization, Investigation, Methodology, Software, Validation, Visualization, Funding acquisition, Writing – original draft. **Anna Bond Estes:** Validation, Writing – review & editing. **Lyndon Despard Estes:** Conceptualization, Funding acquisition, Methodology, Resources, Supervision, Writing – review & editing.

## Declaration of Competing Interest

The authors declare that they have no known competing financial interests or personal relationships that could have appeared to influence the work reported in this paper.

## Data availability

I have shared the data and code link in the manuscript.

## Acknowledgments

This work was supported by the Future Investigators in NASA Earth and Space Science and Technology (FINESST) program (award number: 80NSSC20K1640).

## Appendix A. Supplementary material

Supplementary data to this article can be found online at <https://doi.org/10.1016/j.jag.2022.103152>.

## References

- Abdi, A.M., Brandt, M., Abel, C., Fensholt, R., 2022. Satellite remote sensing of savannas: current status and emerging opportunities. *J. Remote Sens.* 2022, 1–20. [10.34133/2022/9835284](https://doi.org/10.34133/2022/9835284).
- Anderson, S.J., Ankor, B.L., Sutton, P.C., 2017. Ecosystem service valuations of South Africa using a variety of land cover data sources and resolutions. *Ecosyst. Serv.* 27, 173–178. <https://doi.org/10.1016/j.ecoser.2017.06.001>.
- Aquino, C., Mitchard, E.T.A., McNicol, I.M., Carstairs, H., Burt, A., Puma Vilca, B.L., Mayta, S., Disney, M., 2022. Detecting tropical forest degradation using optical satellite data: an experiment in Peru show texture at 3 M gives best results. doi: 10.20944/preprints202202.0141.v1.
- Awuah, K.T., Aplin, P., 2021. Fusion of Sentinel-2 data with high resolution open access planet basemaps for grazing lawn detection in Southern African Savannas. In: 2021 IEEE International Geoscience and Remote Sensing Symposium IGARSS. IEEE. pp. 1409–1412.
- Barsi, Á., Kugler, Z.s., László, I., Szabó, G.y., Abdulmutalib, H.M., 2018. Accuracy dimensions in remote sensing. *Int. Arch. Photogramm. Remote Sens. Spat. Inf. Sci.* XLII-3, 61–67. <https://doi.org/10.5194/isprs-archives-XLII-3-61-2018>.



- Bengio, Y., 2012. Practical recommendations for gradient-based training of deep architectures. In: *Neural Networks: Tricks of the Trade*. Springer, pp. 437–478.
- Breiman, L., 2001. Random forests. *Mach. Learn.* 45, 5–32.
- Brodersen, K.H., Ong, C.S., Stephan, K.E., Buhmann, J.M., 2010. The balanced accuracy and its posterior distribution. In: 2010 20th International Conference on Pattern Recognition. IEEE, pp. 3121–3124.
- Buchhorn, M., Smets, B., Bertels, L., De Roo, B., Lesiv, M., Tsendbazar, N.-E., Herold, M., Fritz, S., 2020b. Copernicus global land service: land cover 100m: collection 3 Epoch 2018, globe. Version V3 01Data Set.
- Buchhorn, M., Lesiv, M., Tsendbazar, N.-E., Herold, M., Bertels, L., Smets, B., 2020a. Copernicus global land cover layers—collection 2. *Remote Sens.* 12, 1044.
- Bullock, E.L., Healey, S.P., Yang, Z., Oduor, P., Gorelick, N., Omondi, S., Ouko, E., Cohen, W.B., 2021. Three decades of land cover change in East Africa. *Land* 10, 150. <https://doi.org/10.3390/land10020150>.
- Burke, M., Lobell, D.B., 2017. Satellite-based assessment of yield variation and its determinants in smallholder agricultural systems. *Proc. Natl. Acad. Sci.* 114, 2189–2194. <https://doi.org/10.1073/pnas.1616919114>.
- Campos-Taberner, M., García-Haro, F.J., Martínez, B., Izquierdo-Verdiguier, E., Atzberger, C., Camps-Valls, G., Gilabert, M.A., 2020. Understanding deep learning in land use classification based on Sentinel-2 time series. *Sci. Rep.* 10, 17188. <https://doi.org/10.1038/s41598-020-74215-5>.
- Chamorro Martínez, J.A., Cué La Rosa, L.E., Feitosa, R.Q., Sanches, I.D., Happ, P.N., 2021. Fully convolutional recurrent networks for multitemporal crop recognition from multitemporal image sequences. *ISPRS J. Photogramm. Remote Sens.* 171, 188–201. <https://doi.org/10.1016/j.isprsjprs.2020.11.007>.
- Chan, J.-C.-W., Paelinckx, D., 2008. Evaluation of Random Forest and Adaboost tree-based ensemble classification and spectral band selection for ecotone mapping using airborne hyperspectral imagery. *Remote Sens. Environ.* 112, 2999–3011. <https://doi.org/10.1016/j.rse.2008.02.011>.
- Cheng, Y., Vrieling, A., Fava, F., Meroni, M., Marshall, M., Gachoki, S., 2020. Phenology of short vegetation cycles in a Kenyan rangeland from PlanetScope and Sentinel-2. *Remote Sens. Environ.* 248, 112004. <https://doi.org/10.1016/j.rse.2020.112004>.
- Congalton, R., Yadav, K., McDonnell, K., Poehnell, J., Stevens, B., Gumma, M., Tuguntla, P., Thenkabail, P., 2017. Global Food Security-support Analysis Data (GFSAD) Cropland Extent 2015 Validation 30 m V001.
- Doggart, N., Morgan-Brown, T., Lyimo, E., Mbilinyi, B., Meshack, C.K., Sallu, S.M., Spracklen, D.V., 2020. Agriculture is the main driver of deforestation in Tanzania. *Environ. Res. Lett.* 15, 034028. <https://doi.org/10.1088/1748-9326/ab6b35>.
- Elmes, A., Alemohammad, H., Avery, R., Caylor, K., Eastman, J., Fishgold, L., Friedl, M., Jain, M., Kohli, D., Laso Bayas, J., Lunga, D., McCarty, J., Pontius, R., Reinmann, A., Rogan, J., Song, L., Stoyanova, H., Ye, S., Yi, Z.-F., Estes, L., 2020. Accounting for training data error in machine learning applied to Earth observations. *Remote Sens.* 12, 1034. <https://doi.org/10.3390/rs12061034>.
- Estes, L.D., Ye, S., Song, L., Luo, B., Eastman, J.R., Meng, Z., Zhang, Q., McRitchie, D., Debats, S.R., Muhando, J., Amukoa, A.H., Kaloo, B.W., Makuru, J., Mbatia, B.K., Muasa, I.M., Mucha, J., Mugami, A.M., Mugami, J.M., Muinde, F.W., Mwawaza, F.M., Ochieng, J., Oduol, C.J., Oduor, P., Wanjiku, T., Wanyoike, J.G., Avery, R.B., Caylor, K.K., 2022. High resolution, annual maps of field boundaries for smallholder-dominated croplands at national scales. *Front. Artif. Intell.* 4, 744863. <https://doi.org/10.3389/frai.2021.744863>.
- Fritz, S., See, L., Rembold, F., 2010. Comparison of global and regional land cover maps with statistical information for the agricultural domain in Africa. *Int. J. Remote Sens.* 31, 2237–2256. <https://doi.org/10.1080/01431690902946598>.
- Fritz, S., You, L., Bun, A., See, L., McCallum, I., Schill, C., Perger, C., Liu, J., Hansen, M., Obersteiner, M., 2011. Cropland for sub-Saharan Africa: a synergistic approach using five land cover data sets. *Geophys. Res. Lett.* 38.
- Gómez, C., White, J.C., Wulder, M.A., 2016. Optical remotely sensed time series data for land cover classification: a review. *ISPRS J. Photogramm. Remote Sens.* 116, 55–72. <https://doi.org/10.1016/j.isprsjprs.2016.03.008>.
- Gong, P., Liu, H., Zhang, M., Li, C., Wang, J., Huang, H., Clinton, N., Ji, L., Li, W., Bai, Y., Chen, B., Xu, B., Zhu, Z., Yuan, C., Ping Suen, H., Guo, J., Xu, N., Li, W., Zhao, Y., Yang, J., Yu, C., Wang, X., Fu, H., Yu, L., Dronova, I., Hui, F., Cheng, X., Shi, X., Xiao, F., Liu, Q., Song, L., 2019. Stable classification with limited sample: transferring a 30-m resolution sample set collected in 2015 to mapping 10-m resolution global land cover in 2017. *Sci. Bull.* 64, 370–373. <https://doi.org/10.1016/j.scib.2019.03.002>.
- Houborg, R., McCabe, M.F., 2018. A cubesat enabled spatio-temporal enhancement method (CESTEM) utilizing Planet, Landsat and MODIS data. *Remote Sens. Environ.* 209, 211–226. <https://doi.org/10.1016/j.rse.2018.02.067>.
- Huete, A.R., 1988. A soil-adjusted vegetation index (SAVI). *Remote Sens. Environ.* 25, 295–309. [https://doi.org/10.1016/0034-4257\(88\)90106-X](https://doi.org/10.1016/0034-4257(88)90106-X).
- Iglovikov, V., Mushinskiy, S., Osin, V., 2017. Satellite imagery feature detection using deep convolutional neural network: a Kaggle competition.
- Jacob, A.W., Vicente-Guijalba, F., Lopez-Martinez, C., Lopez-Sanchez, J.M., Litzinger, M., Kristen, H., Mestre-Quereda, A., Ziolkowski, D., Laval, M., Notarnicola, C., Suresh, G., Antropov, O., Ge, S., Praks, J., Ban, Y., Pottier, E., Mallorqui Franquet, J. J., Duro, J., Engdahl, M.E., 2020. Sentinel-1 InSAR coherence for land cover mapping: a comparison of multiple feature-based classifiers. *IEEE J. Sel. Top. Appl. Earth Obs. Remote Sens.* 13, 535–552. <https://doi.org/10.1109/JSTARS.2019.2958847>.
- Jiang, Z., Huete, A.R., Didan, K., Miura, T., 2008. Development of a two-band enhanced vegetation index without a blue band. *Remote Sens. Environ.* 112, 3833–3845.
- Jin, Z., Azzari, G., You, C., Di Tommaso, S., Aston, S., Burke, M., Lobell, D.B., 2019. Smallholder maize area and yield mapping at national scales with Google Earth Engine. *Remote Sens. Environ.* 228, 115–128. <https://doi.org/10.1016/j.rse.2019.04.016>.
- Kaufman, Y.J., Tanre, D., 1992. Atmospherically resistant vegetation index (ARVI) for EOS-MODIS. *IEEE Trans. Geosci. Remote Sens.* 30, 261–270.
- Kerner, H., Tseng, G., Becker-Reshef, I., Nakalembe, C., Barker, B., Munshell, B., Paliyam, M., Hosseini, M., 2020. Rapid Response Crop Maps in Data Sparse Regions. *ArXiv200616866 Cs Eess*.
- Laso Bayas, J.C., Lesiv, M., Waldner, F., Schucknecht, A., Duerauer, M., See, L., Fritz, S., Fraisl, D., Moorthy, I., McCallum, I., Perger, C., Danylo, O., Defourny, P., Gallego, J., Gilliams, S., Akhtar, I.H., Baishya, S.J., Baruah, M., Bungnamei, K., Campos, A., Changkakati, T., Cipriani, A., Das, Krishna, Das, Keemee, Das, I., Davis, K.F., Hazarika, P., Johnson, B.A., Malek, Z., Molinari, M.E., Panging, K., Pawe, C.K., Pérez-Hoyos, A., Sahariah, P.K., Sahariah, D., Saikia, A., Saikia, M., Schlesinger, P., Seidacaru, E., Singha, K., Wilson, J.W., 2017. A global reference database of crowdsourced cropland data collected using the Geo-Wiki platform. *Sci. Data* 4, 170136. <https://doi.org/10.1038/sdata.2017.136>.
- Leite-Filho, A.T., Soares-Filho, B.S., Davis, J.L., Abrahão, G.M., Börner, J., 2021. Deforestation reduces rainfall and agricultural revenues in the Brazilian Amazon. *Nat. Commun.* 12, 2591. <https://doi.org/10.1038/s41467-021-22840-7>.
- Long, J., Shelhamer, E., Darrell, T., 2015. Fully convolutional networks for semantic segmentation. In: *Proceedings of the IEEE Conference on Computer Vision and Pattern Recognition*, pp. 3431–3440.
- Luo, L., Xiong, Y., Liu, Y., Sun, X., 2019. Adaptive Gradient Methods with Dynamic Bound of Learning Rate. *ArXiv190209843 Cs Stat*.
- Moody, A., Johnson, D.M., 2001. Land-surface phenologies from AVHRR using the discrete Fourier transform. *Remote Sens. Environ.* 75, 305–323. [https://doi.org/10.1016/S0034-4257\(00\)00175-9](https://doi.org/10.1016/S0034-4257(00)00175-9).
- Norway's International Climate and Forest Initiative (NICFI) [WWW Document], 2020. NICFI. URL <https://www.nicfi.no/> (accessed 4.17.22).
- Olofsson, P., Foody, G.M., Herold, M., Stehman, S.V., Woodcock, C.E., Wulder, M.A., 2014. Good practices for estimating area and assessing accuracy of land change. *Remote Sens. Environ.* 148, 42–57. <https://doi.org/10.1016/j.rse.2014.02.015>.
- Pascual, A., Tupinambá-Simões, F., de Conto, T., 2022. Using multi-temporal tree inventory data in eucalypt forestry to benchmark global high-resolution canopy height models. A showcase in Mato Grosso, Brazil. *Ecol. Inform.* 70, 101748. doi: 10.1016/j.ecoinf.2022.101748.
- Perez, L., Wang, J., 2017. The effectiveness of data augmentation in image classification using deep learning. *ArXiv Prepr. ArXiv171204621*.
- Pérez-Hoyos, A., Udiás, A., Rembold, F., 2020. Integrating multiple land cover maps through a multi-criteria analysis to improve agricultural monitoring in Africa. *Int. J. Appl. Earth Obs. Geoinformation* 88, 102064. <https://doi.org/10.1016/j.jag.2020.102064>.
- Pettorelli, N., Wegmann, M., Skidmore, A., Múcher, S., Dawson, T.P., Fernandez, M., Lucas, R., Schaepman, M.E., Wang, T., O'Connor, B., Jongman, R.H.G., Kempeneers, P., Sonnenschein, R., Leidner, A.K., Böhm, M., He, K.S., Nagendra, H., Dubois, G., Fatoyinbo, T., Hansen, M.C., Paganini, M., de Klerk, H.M., Asner, G.P., Kerr, J.T., Estes, A.B., Schmeller, D.S., Heiden, U., Rocchini, D., Pereira, H.M., Turak, E., Fernandez, N., Lausch, A., Cho, M.A., Alcaraz-Segura, D., McGeoch, M.A., Turner, W., Mueller, A., St-Louis, V., Penner, J., Vihervaara, P., Belward, A., Reyers, B., Geller, G.N., 2016. Framing the concept of satellite remote sensing essential biodiversity variables: challenges and future directions. *Remote Sens. Ecol. Conserv.* 2, 122–131. <https://doi.org/10.1002/rse2.15>.
- Planet Team, 2017. Planet application program interface: In space for life on Earth. San Franc. CA 2017, 40.
- Rakhlin, A., Davydov, A., Nikolenko, S., 2018. Land Cover Classification from Satellite Imagery with U-Net and Lovász-Softmax Loss. In: 2018 IEEE/CVF Conference on Computer Vision and Pattern Recognition Workshops (CVPRW). Presented at the 2018 IEEE/CVF Conference on Computer Vision and Pattern Recognition Workshops (CVPRW), IEEE, Salt Lake City, UT, USA. pp. 257–2574. doi: 10.1109/CVPRW.2018.00048.
- Reiner, F., Brandt, M., Tong, X., Skole, D., Kariryaa, A., Ciaia, P., Davies, A., Hiernaux, P., Chave, J., Mugabowindekwe, M., Igel, C., Oehmcke, S., Gieseke, F., Li, S., Liu, S., Saatchi, S., Boucher, P., Singh, J., Taourdeau, S., Dendoncker, M., Song, X.-P., Mertz, O., Tucker, C.J., Fensholt, R., 2022. More than one quarter of Africa's tree cover found outside areas previously classified as forest. doi: 10.21203/rs.3.rs-1816495/v2.
- Ren, H., Liu, Y., Chang, X., Yang, J., Xiao, X., Huang, X., 2022. mapping high-resolution global impervious surface area: status and trends. *IEEE J. Sel. Top. Appl. Earth Obs. Remote Sens.* 1–21. <https://doi.org/10.1109/JSTARS.2022.3201380>.
- Rienow, A., Schweighöfer, J., Dedering, T., Goebel, M., Graw, V., 2022. Detecting land use and land cover change on Barbuda before and after the Hurricane Irma with respect to potential land grabbing: a combined volunteered geographic information and multi sensor approach. *Int. J. Appl. Earth Obs. Geoinformation* 108, 102732. <https://doi.org/10.1016/j.jag.2022.102732>.
- Ronneberger, O., Fischer, P., Brox, T., 2015. U-net: Convolutional networks for biomedical image segmentation. In: *International Conference on Medical Image Computing and Computer-Assisted Intervention*. Springer, pp. 234–241.
- Roy, D.P., Huang, H., Houborg, R., Martins, V.S., 2021. A global analysis of the temporal availability of PlanetScope high spatial resolution multi-spectral imagery. *Remote Sens. Environ.* 264, 112586. <https://doi.org/10.1016/j.rse.2021.112586>.
- Rufin, P., Bey, A., Picoli, M., Meyfroidt, P., 2022. Large-area mapping of active cropland and short-term fallows in smallholder landscapes using PlanetScope data. *Int. J. Appl. Earth Obs. Geoinformation* 112, 102937. <https://doi.org/10.1016/j.jag.2022.102937>.
- Schmitt, M., Hughes, L.H., Qiu, C., Zhu, X.X., 2019. SEN12MS – a curated dataset of georeferenced multi-spectral Sentinel-1/2 imagery for deep learning and data fusion. *ISPRS Ann. Photogramm. Remote Sens. Spat. Inf. Sci.* IV-2/W7, 153–160. <https://doi.org/10.5194/isprs-annals-IV-2-W7-153-2019>.

- Sebastian, K., 2009. Agro-ecological Zones of Africa.
- Sheykhoum, M., Mahdianpari, M., Ghanbari, H., Mohammadimanesh, F., Ghamisi, P., Homayouni, S., 2020. Support vector machine versus random forest for remote sensing image classification: a meta-analysis and systematic review. *IEEE J. Sel. Top. Appl. Earth Obs. Remote Sens.* 13, 6308–6325. <https://doi.org/10.1109/JSTARS.2020.3026724>.
- Shorten, C., Khoshgoftaar, T.M., 2019. A survey on image data augmentation for deep learning. *J. Big Data* 6, 1–48.
- Smith, L.N., 2017. Cyclical learning rates for training neural networks. In: 2017 IEEE Winter Conference on Applications of Computer Vision (WACV). IEEE, pp. 464–472.
- Solbrig, O.T., 1996. The diversity of the savanna ecosystem. In: *Biodiversity and Savanna Ecosystem Processes*. Springer, pp. 1–27.
- Solórzano, J.V., Mas, J.F., Gao, Y., Gallardo-Cruz, J.A., 2021. Land use land cover classification with U-Net: advantages of combining Sentinel-1 and Sentinel-2 imagery. *Remote Sens.* 13, 3600. <https://doi.org/10.3390/rs13183600>.
- Song, X.-P., Hansen, M.C., Stehman, S.V., Potapov, P.V., Tyukavina, A., Vermote, E.F., Townshend, J.R., 2018. Global land change from 1982 to 2016. *Nature* 560, 639–643. <https://doi.org/10.1038/s41586-018-0411-9>.
- Sugimoto, R., Kato, S., Nakamura, R., Tsutsumi, C., Yamaguchi, Y., 2022. Deforestation detection using scattering power decomposition and optimal averaging of volume scattering power in tropical rainforest regions. *Remote Sens. Environ.* 275, 113018 <https://doi.org/10.1016/j.rse.2022.113018>.
- Sun, R.-Y., 2020. Optimization for deep learning: an overview. *J. Oper. Res. Soc. China* 8, 249–294.
- Talukdar, S., Singha, P., Mahato, S., Shahfahad, P.S., Liou, Y.-A., Rahman, A., 2020. Land-use land-cover classification by machine learning classifiers for satellite observations—a review. *Remote Sens.* 12, 1135. <https://doi.org/10.3390/rs12071135>.
- Tong, X.-Y., Xia, G.-S., Lu, Q., Shen, H., Li, S., You, S., Zhang, L., 2020. Land-cover classification with high-resolution remote sensing images using transferable deep models. *Remote Sens. Environ.* 237, 111322 <https://doi.org/10.1016/j.rse.2019.111322>.
- Torres, R., Snoeijs, P., Geudtner, D., Bibby, D., Davidson, M., Attema, E., Potin, P., Rommen, B., Flourey, N., Brown, M., et al., 2012. GMES Sentinel-1 mission. *Remote Sens. Environ.* 120, 9–24.
- Torrey, L., Shavlik, J., 2010. Transfer learning. In: *Handbook of Research on Machine Learning Applications and Trends: Algorithms, Methods, and Techniques*. IGI global, pp. 242–264.
- Tsalyuk, M., Kelly, M., Getz, W.M., 2017. Improving the prediction of African savanna vegetation variables using time series of MODIS products. *ISPRS J. Photogramm. Remote Sens.* 131, 77–91. <https://doi.org/10.1016/j.isprsjprs.2017.07.012>.
- Tucker, C.J., 1979. Red and photographic infrared linear combinations for monitoring vegetation. *Remote Sens. Environ.* 8, 127–150.
- Vizzari, M., 2022. PlanetScope, Sentinel-2, and Sentinel-1 Data integration for object-based land cover classification in Google Earth Engine. *Remote Sens.* 14, 2628. <https://doi.org/10.3390/rs14112628>.
- Volpi, M., Tuia, D., 2016. Dense semantic labeling of subdecimeter resolution images with convolutional neural networks. *IEEE Trans. Geosci. Remote Sens.* 55, 881–893.
- Walsh, M., Meliyo, J., Awiti, A., Scott, B., Walsh, B., Macmillan, B., 2018. Tanzania Soil Information Service (TanSIS).
- Wang, S., Chen, W., Xie, S.M., Azzari, G., Lobell, D.B., 2020. Weakly supervised deep learning for segmentation of remote sensing imagery. *Remote Sens.* 12, 207. <https://doi.org/10.3390/rs12020207>.
- Whitley, R., Beringer, J., Hutley, L.B., Abramowitz, G., De Kauwe, M.G., Evans, B., Haverd, V., Li, L., Moore, C., Ryu, Y., et al., 2017. Challenges and opportunities in land surface modelling of savanna ecosystems. *Biogeosciences* 14, 4711–4732.
- Xu, Y., Yu, L., Feng, D., Peng, D., Li, C., Huang, X., Lu, H., Gong, P., 2019. Comparisons of three recent moderate resolution African land cover datasets: CGLS-LC100, ESA-S2-LC20, and FROM-GLC-Africa30. *Int. J. Remote Sens.* 40, 6185–6202.
- Yang, J., Huang, X., 2021. 30 m annual land cover and its dynamics in China from 1990 to 2019. *Earth Syst. Sci. Data Discuss* 2021, 1–29.
- Zhang, W., Brandt, M., Wang, Q., Prishchepov, A.V., Tucker, C.J., Li, Y., Lyu, H., Fensholt, R., 2019. From woody cover to woody canopies: how Sentinel-1 and Sentinel-2 data advance the mapping of woody plants in savannas. *Remote Sens. Environ.* 234, 111465 <https://doi.org/10.1016/j.rse.2019.111465>.
- Zhang, X., Liu, L., Chen, X., Gao, Y., Xie, S., Mi, J., 2021. GLC\_FCS30: global land-cover product with fine classification system at 30 m using time-series Landsat imagery. *Earth Syst. Sci. Data* 13, 2753–2776. <https://doi.org/10.5194/essd-13-2753-2021>.